Front. Earth Sci. 2018, 12(2): 444–456
https://doi.org/10.1007/s11707-017-0657-9

RESEARCH ARTICLE

Analysis of relationships between land surface temperature and land use changes in the Yellow River Delta

Jicai NING (✉)[1], Zhiqiang GAO[1], Ran MENG[2], Fuxiang XU[1], Meng GAO[1]

1 Yantai Institute of Coastal Zone Research, Chinese Academy of Sciences, Yantai 264003, China
2 Environmental & Climate Sciences Department, Brookhaven National Laboratory, Upton, NY 11973, USA

Abstract This study analyzed land use and land cover changes and their impact on land surface temperature using Landsat 5 Thematic Mapper and Landsat 8 Operational Land Imager and Thermal Infrared Sensor imagery of the Yellow River Delta. Six Landsat images comprising two time series were used to calculate the land surface temperature and correlated vegetation indices. The Yellow River Delta area has expanded substantially because of the deposited sediment carried from upstream reaches of the river. Between 1986 and 2015, approximately 35% of the land use area of the Yellow River Delta has been transformed into salterns and aquaculture ponds. Overall, land use conversion has occurred primarily from poorly utilized land into highly utilized land. To analyze the variation of land surface temperature, a mono-window algorithm was applied to retrieve the regional land surface temperature. The results showed bilinear correlation between land surface temperature and the vegetation indices (i.e., Normalized Difference Vegetation Index, Adjusted-Normalized Vegetation Index, Soil-Adjusted Vegetation Index, and Modified Soil-Adjusted Vegetation Index). Generally, values of the vegetation indices greater than the inflection point mean the land surface temperature and the vegetation indices are correlated negatively, and vice versa. Land surface temperature in coastal areas is affected considerably by local seawater temperature and weather conditions.

Keywords land surface temperature, mono-window algorithm, Yellow River Delta, land use change, vegetation index

Received October 17, 2016; accepted March 31, 2017

E-mail: jcning@yic.ac.cn

1 Introduction

Land surface temperature (LST) is one of the key parameters that control the physical, chemical, and biological processes on Earth (Pu et al., 2006). Many studies of Earth's environment and resources have depended on LST as fundamental data. Remote sensing is a practical approach for the retrieval of LSTs across large spatial and temporal scales. The LSTs acquired by satellite-borne sensors have been used in numerous heat-balance, climate-modeling, and global-change-monitoring studies (Bhattacharya et al., 2010; Fall et al., 2010). Planck's law is used for calculating brightness temperature from the atmospheric radiances obtained from thermal infrared sensors (Dash et al., 2002). The brightness temperature is converted into LST using ground surface emissivity with consideration of vegetation density, the roughness and thermal properties of the ground surface, and water content of the soil (Friedl, 2002). Different methods and algorithms have been developed to retrieve LSTs from data acquired by the Landsat Thematic Mapper and Enhanced Thematic Mapper Plus sensors that operate with only one thermal band (Qin et al., 2001a; Sobrino et al., 2004; Weng et al., 2004). Using only the near-surface air temperature and water vapor content instead of atmospheric profiles, Qin's mono-window algorithm can improve LST retrievals from Landsat imagery with only one thermal band (Li et al., 2013; Windahl and Beurs, 2016). Considering the two thermal bands of the Landsat 8 Thermal Infrared Sensor, Rozenstein et al. (2014) discussed the feasibility and the related parameters of the split-window algorithm in LST retrieval. Jimenez-Munoz et al. (2014) contrasted the single-channel algorithm and the split-window algorithm in LST inversion, and they found the accuracy of the split-window algorithm slightly better than the mono-window algorithm in association with higher water vapor contents.

Land use and land cover changes (LUCC) have been reported being among the main drivers of environmental

change and they can be affected by climate change and climate variability (Pielke Sr. et al., 1998; Brunsell, 2006). Research on the relationship between LST and land use type has shown the main drivers inducing complicated land use conversions are population increase and economic development. Furthermore, LST change has been found to be correlated spatially with LUCC (Wang et al., 2016). Studies have shown strong correlation between surface/air temperature and different land use types (Yokohari et al., 2001; Chen et al., 2006; Cheng et al., 2008). The LST and energy balance can be affected by vegetation, which influences the land–air exchange of energy and water (Kumar and Shekhar, 2015). Based on different spatial sampling methods, Sahana et al. (2016) and Rhee et al. (2014) analyzed the relationship between LST and land use changes. To investigate the driving mechanisms of energy exchange and LST, increasing emphasis has been placed on research into the vegetation–LST relationship (Petropoulos et al., 2014). As important indicators of land use and vegetation, vegetation indices (VIs), including the Normalized Difference Vegetation Index (NDVI), Ratio Vegetation Index (RVI), and Soil-Adjusted Vegetation Index (SAVI), have been used widely to investigate the vegetation–LST relationship (Yue et al., 2007; Wei and Zhou, 2011). Lv and Zhou (2011) examined the correlation between LST and VIs based on four transects across a study area. Their results indicated an evident heat island effect caused by urban areas, while a cool island effect was related mainly to the abundance of water and vegetation. Most studies of the relationships between LST and VIs have been conducted using certain profiles (Yue et al., 2007; Buyadi et al., 2013; Kumar and Shekhar, 2015; Pal and Ziaul, 2017). Although the selection of a certain profile can simplify the analytical process, inappropriate profile selection could lead to biased or random results.

Given the background of land use change, the objective of this study was to investigate the relationship between satellite-retrieved LSTs and VIs based on average values obtained via spatial overlay analysis on the regional scale instead of using certain profiles.

2 Materials and methods

2.1 Study area

The Yellow River Delta (YRD) has received increasing attention from scientists, engineers, and environmental planners because of its critical role in wildlife protection, energy production, and agriculture (Zhang et al., 2016). On the western coast of the Bohai Sea, the study area (37°01′ N–38°11′N, 118°04′E–118°21′E) in Shandong Province has the largest and youngest coastal wetland ecosystem in China, which encompassed an area of about 11,473 km^2 in 2015 (Fig. 1). The elevation of the study area ranges from 0–45 m a.s.l. The regional climate is controlled by the East Asian monsoon system; summer is warm and wet, while winter is cold and dry. The average annual temperature is 12.1°C, with monthly means ranging from a minimum of −1.3°C in December to a maximum of 27.7°C in August (Jin et al., 2016).

The YRD is highly dynamic, and it is experiencing rapid urban and industrial development (Ottinger et al., 2013). Like many of the large deltas around the world (Blum and Roberts, 2009; Syvitski et al., 2009), the YRD is facing increasing risk of degradation due to both anthropogenic and natural forces (Cui et al., 2009; Bi et al., 2014; Gao et al., 2014; Kong et al., 2015). Recently, with the expansion of reclamation activities, natural systems in areas of the YRD, especially wetland ecosystems, have been suffering severe disturbance (Jin et al., 2016). Population growth, oil and gas extraction, and agricultural development have all placed enormous demands on the land and water resources of the YRD, and they have modified the natural geological, hydrological, and ecological systems of the area (Wang et al., 2006). With continued acceleration of economic development and urbanization, the demand for land to service port construction, construction of tidal embankments, aquaculture, land reclamation, and road construction has increased steadily.

2.2 Data preparation

Two time series of Landsat images in the dry season were downloaded from the USGS website (http://earthexplorer.usgs.gov/) as the main data for the comparative study of LST and VIs in the YRD. The acquisition date and the details of the sensor and thermal band used for the retrievals are listed in Table 1. Time series A was selected just before the wet season with similar daily order, and time series B was after the wet season. After atmospheric and radiometric corrections, the remote sensing data were used for both calculating VIs and retrieving LSTs. Two images with maximum time span in series A were used to analyze the overall trend of regional land use change and LST change over nearly 30 years. Then, six images from both time series were used to analyze the relationship between LST and the VIs. Necessary meteorological data including temperature, wind speed, relative humidity, and precipitation were obtained from the China Meteorological Data Network (http://data.cma.cn/). Using the inverse distance weighting interpolation method, relevant meteorological raster data of the study area were acquired from internal and surrounding observations. All data were georeferenced to a common UTM coordinate system (WGS_1984_UTM_Zone_50N) and re-sampled using the nearest-neighbor algorithm with a pixel size of 30 m× 30 m.

The LULC (Land Use and Land Cover) data were extracted using automatic computer classification, aided by manual interpretation according to the classification system. In this study, both supervised classification and

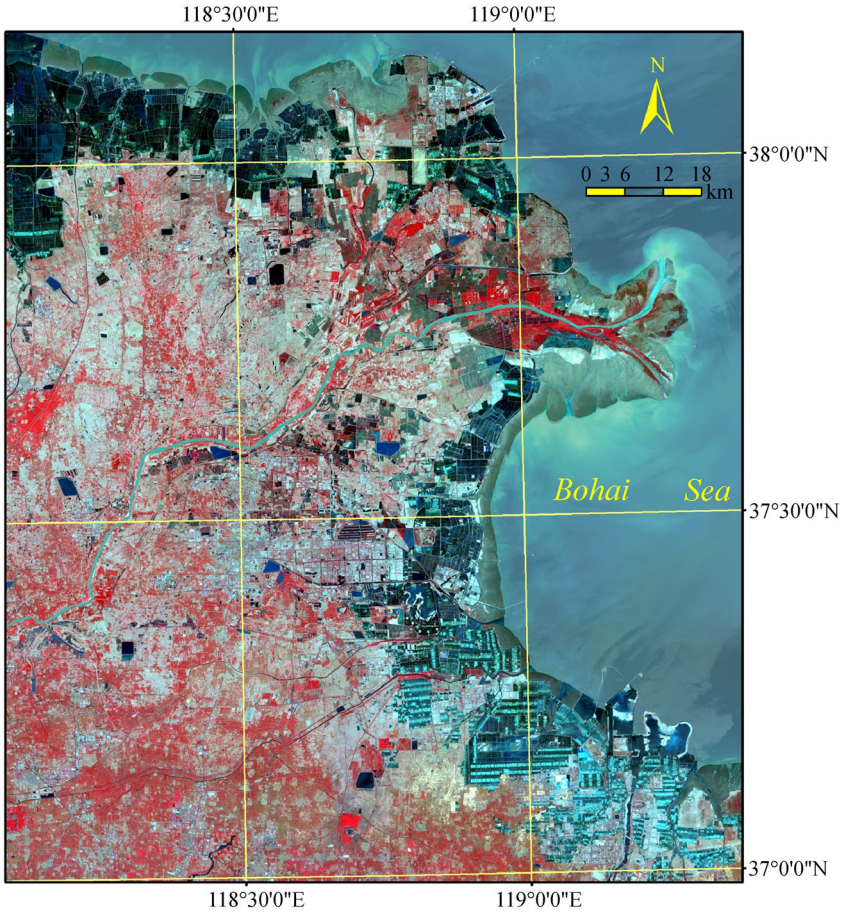

Fig. 1 Location of study area (standard pseudocolor Landsat image, June 5, 2015).

Table 1 List of Landsat images used for the two time series

Time series	Date acquired	Satellite	Sensors	Thermal band used
A (before wet season)	6/5/1986	Landsat 5	TM	Band 6
	5/31/1996	Landsat 5	TM	Band 6
	6/5/2015	Landsat 8	OLI/TIRS	Band 10
B (after wet season)	10/5/1984	Landsat 5	TM	Band 6
	10/2/2006	Landsat 5	TM	Band 6
	10/5/2013	Landsat 8	OLI/TIRS	Band 10

maximum likelihood methods were applied to extract land use information with consideration of the spectral characteristics of ground objects and the situation of the YRD area in particular. Finally, a decision tree classification model was established to acquire the land use map for the research area. The overall accuracy was up to 95%, as verified by matching with field visits and literature values.

2.3 Retrieval of LST

Atmospheric and radiometric corrections are necessary before LST retrieval. Radiometric correction is applied to convert the digital number (DN) into top of atmosphere spectral radiance according to related parameters. The following equation developed by the National Aeronautics and Space Administration is generally used to compute the spectral radiance from DN values of Thematic Mapper™; data (Qin et al., 2001a):

$$L_{(\lambda)} = L_{\min(\lambda)} + \left(L_{\max(\lambda)} - L_{\min(\lambda)}\right) Q_{\mathrm{dn}} / Q_{\max}, \quad (1)$$

where $L_{(\lambda)}$ is the spectral radiance received by the sensor ($\mathrm{mW \cdot cm^{-2} \cdot sr^{-1} \cdot \mu m^{-1}}$), $Q_{\max}$ is the maximum DN value with $Q_{\max} = 255$, Q_{dn} is the grayscale level for the analyzed

pixel of the TM image, and $L_{\min(\lambda)}$ and $L_{\max(\lambda)}$ are the minimum and maximum detected spectral radiances for $Q_{\mathrm{dn}} = 0$ and $Q_{\mathrm{dn}} = 255$, respectively. For a detailed explanation of the process for calculating radiance in relation to Landsat 8 Operational Land Imager and Thermal Infrared Sensor (OLI/TIRS) data, please refer to related websites (e.g., https://landsat.usgs.gov/using-usgs-landsat-8-product).

In order to obtain accurate reflectance data, atmospheric correction of the Landsat data was performed by combining a lookup table and a dark-object method (Liang et al., 2002).

Because of the larger calibration uncertainty associated with Band 11 (USGS, 2014), the use of a split-window algorithm that relies on Band 11 data is not recommended for LST retrieval. For methods using single bands, the LST estimated from Band 10 (with weaker absorption) has higher accuracy than Band 11 (Jimenez-Munoz et al., 2014; Yu et al., 2014). To obtain comparable results from different sensors, a mono-window algorithm (Qin et al., 2001a) was employed to retrieve the LST throughout different years. Band 6 of the TM and Band 10 of the TIRS were used as thermal bands for LST retrieval.

The mono-window algorithm for LST retrieval from the thermal band data of Landsat assumes the brightness temperature of the thermal band at the satellite level can be computed from the data. According to the radiance transfer equation, Taylor's expansion to the Planck function has to be applied. Qin et al. (2001b) derived an approximate expression for LST retrieval, suitable for thermal band data, by simplifying the relationship between radiance and brightness temperature with a linear regression, which can be expressed as Eq. (2):

$$T_s = \{a_6(1-C_6-D_6) + [b_6(1-C_6-D_6) + C_6 + D_6]T_6 - D_6T_a\}/C_6, \quad (2)$$

where T_s is the LST (K), T_6 is the brightness temperature (K) (Band 6 for Landsat 5, Bands 10 or 11 for Landsat 8), a_6 and b_6 are the regression coefficients between T_6 and C_6, and T_a is the average effective mean atmospheric temperature (K). In practice, the possible temperature range of LST is 0–70°C, a_6 = –67.35535 and b_6 = 0.458608. Coefficients C_6 and D_6 coefficients defined as below in Eqs. (3) and (4), respectively:

$$C_6 = \varepsilon_6\tau_6, \quad (3)$$

$$D_6 = (1-\tau_6)[1 + (1-\varepsilon_6)\tau_6], \quad (4)$$

where τ_6 is the atmospheric transmittance (dimensionless), and ε_6 is the ground emissivity (dimensionless), both at Band 6. It is possible to calculate τ_6 approximately from relative humidity and temperature data (Qin et al., 2001a), and ε_6 can be derived from the relevant vegetation index (Qin et al., 2004).

2.4 Calculation of NDVI, ANDVI, SAVI, and MSAVI

The NDVI is defined as:

$$\mathrm{NDVI} = \frac{\rho_{\mathrm{nir}} - \rho_{\mathrm{red}}}{\rho_{\mathrm{nir}} + \rho_{\mathrm{red}}}, \quad (5)$$

where ρ_{nir} is the reflectance for the near infrared band (Landsat 5 Band 4, Landsat 8 Band 5), and ρ_{red} is the reflectance for the red band (Landsat 5 Band 3, Landsat 8 Band 4).

Based on the NDVI, the reflectances of the blue and green bands were combined to produce the Adjusted-Normalized Difference Vegetation Index (ANDVI). The ANDVI should describe vegetation better than the NDVI under certain conditions (Liu et al., 2008):

$$\mathrm{ANDVI} = \frac{\rho_{\mathrm{nir}} - \rho_{\mathrm{red}} + (1+L)(\rho_{\mathrm{green}} - \rho_{\mathrm{blue}})}{\rho_{\mathrm{nir}} + \rho_{\mathrm{red}} + (1+L)(\rho_{\mathrm{green}} + \rho_{\mathrm{blue}})}, \quad (6)$$

where ρ_{nir}, ρ_{red}, ρ_{green}, and ρ_{blue} are the reflectances for the corresponding bands, and L is the adjusted factor, which is set to reduce soil noise (L = 0.5).

The SAVI and Modified SAVI (MSAVI) are two other VIs used to minimize soil brightness influence (Huete, 1988; Qi et al., 1994):

$$\mathrm{SAVI} = \frac{\rho_{\mathrm{nir}} - \rho_{\mathrm{red}}}{\rho_{\mathrm{nir}} + \rho_{\mathrm{red}} + L}(1+L), \quad (7)$$

$$\mathrm{MSAVI} = \frac{1}{2} \times \left[(2\rho_{\mathrm{nir}}+1) - \sqrt{(2\rho_{\mathrm{nir}}+1)^2 - 8(\rho_{\mathrm{nir}} - \rho_{\mathrm{red}})}\right], \quad (8)$$

where ρ_{nir} and ρ_{red} are the reflectances of the near infrared and red bands, respectively, and L is the adjusted factor (L = 0.5).

3 Results and analysis

3.1 Land use changes in the past 30 years

The Landsat 8 image obtained on June 5, 2015 was corrected geometrically based on the Landsat 5 remote sensing image of the same day in 1986. Land use maps were extracted for two stages in accordance with classification criteria using the corrected remote sensing image.

Figure 2 and Table 2 show that the land area in the research area increased by 205.81 km^2 during the 30-year period 1986–2015 because of sea–land interaction and sediment deposition. Land use was classified into 10 types, as shown in Table 2. The gross area in 1986 was 11,267.69 km^2, and farmland accounted for the largest proportion (55.18%), followed by grassland and beaches. Saline-alkali fields also covered a large area, which accounted for

6.85% of the total. Aquaculture ponds covered a small area, accounting for only 0.65% of the total. Compared with 1986, evident changes in the land use types had occurred by 2015. The greatest increases in area were found for salterns and aquaculture ponds, i.e., 1303.07 and 582.66 km^2, respectively. Their total areal proportion also increased sharply from 2.51% to 18.90% during the 30-year period. To varying degrees, farmland, built-up, and water areas all increased. However, the area of wetlands decreased by 205.34 km^2, accounting for around two-thirds of the original wetland area.

More than one third of the area of regional land use types was changed from 1986 to 2015. Despite an increase in the gross area of farmland, nearly 600 km^2 was transformed into other types (mainly built-up areas, salterns, and aquaculture ponds) (Fig. 2 and Table 3). The increase in farmland area was caused mainly by the development and utilization of grassland, wetland, and saline-alkali land. Grassland was converted mainly into salterns and aquaculture ponds. Although the wetland area is small, the land use changed severely. Nearly 89% of wetland area has been converted into other land use types during the past 30 years, mainly being developed for farmland, salterns, and aquaculture ponds. The diversity of wetland conversion modes also proves the fragility of wetland ecosystems. Saline-alkali fields are distributed mainly on the coast and they have been converted primarily into salterns, aquaculture ponds, and farmland. In particular, 409.93 km^2 was

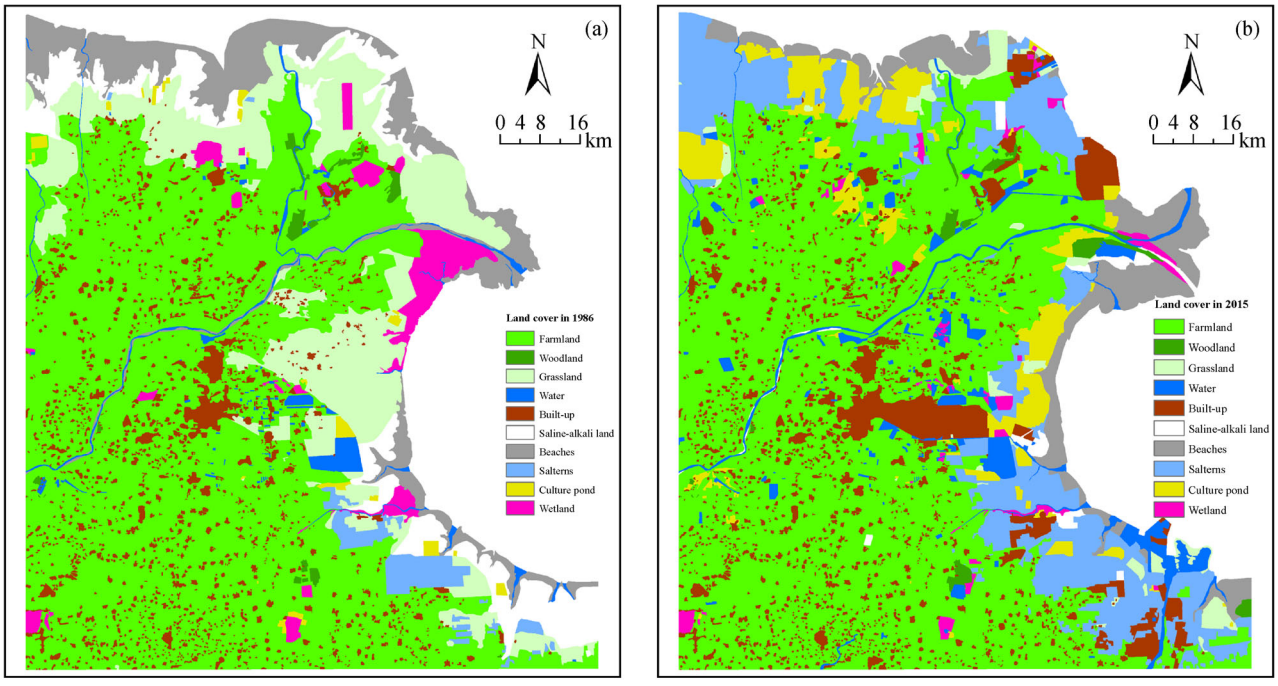

Fig. 2 Distribution maps of land use on June 5, 1986 and 2015.

Table 2 Area and percentage of various land use and land cover types

Land cover type	1986		2015	
	Area/km^2	Percentage/%	Area/km^2	Percentage/%
Farmland	6217.90	55.18	6634.64	56.08
Woodland	65.91	0.58	97.43	0.85
Grassland	1772.91	15.73	194.34	1.69
Water	194.26	1.72	475.89	4.15
Built-up	722.79	6.41	1117.77	10.27
Saline-alkali field	771.79	6.85	76.79	0.67
Beaches	906.25	8.04	720.34	6.28
Salterns	209.41	1.86	1512.48	13.18
Aquaculture ponds	73.20	0.65	655.86	5.72
Wetland	333.28	2.96	127.94	1.12
Total	11,267.691	100	11473.5	100

converted into salterns, accounting for 55% of the total conversion area. The water body area nearly doubled in the 30-year period, which was converted mainly from farmland, grassland, and wetland.

3.2 LST changes in the past 30 years

The surface temperature profile of the research area was retrieved based on the mono-window algorithm of Qin et al. (2001a). Figure 3 shows the spatial distribution of LST on June 5, 1986 and 2015.

The regional mean LST was 36.89°C on June 5, 1986, and 35.41°C on June 5, 2015; the overall decline was 1.48°C. Without considering the impact of other factors such as climate change, the decrease of LST is consistent with the land use changes of expanded water area and increased vegetation coverage. The development of the coastal zone area has promoted more land for use as salterns, aquaculture ponds, and farmland. The increased proportions of aquaculture ponds and water areas have decreased the mean LST of the area to some extent. According to the distribution maps, LST is usually lower in

Table 3 Land use change matrix (from 1986 to 2015)

Land use type	Farmland	Woodland	Grassland	Water	Built-up	Saline-alkali field	Beaches	Salterns	Aquaculture Ponds	Wetland	Year 1986
Farmland	5615.28	10.35	5.56	110.89	160.73	3.04		149.53	137.57	24.95	6217.90
Woodland	21.49	42.32		0.59	0.39			0.04	0.34	0.74	65.91
Grassland	621.36	2.51	92.78	53.96	193.94	7.89	89.64	423.76	251.35	35.72	1772.91
Water	29.88	2.67	1.35	131.99	9.42	0.04	11.52	0.98	1.92	4.48	194.25
Built-up				0.61	722.09			0.09			722.79
Saline-alkali field	48.05	9.40	62.82	17.08	33.55	21.25	67.79	409.30	96.92	3.79	769.93
Beaches	20.51	4.18	8.79	34.81	16.22	9.57	315.61	264.68	91.60	14.09	780.06
Salterns	2.03				28.97	1.25		174.90	2.25		209.41
Aquaculture ponds	8.54		0.64	0.41	0.11			20.57	38.34	4.59	73.20
Wetland	67.50	26.01	8.15	40.70	2.10	33.75	29.34	52.29	35.58	37.86	333.28
Year 2015	6434.64	97.43	180.08	391.02	1167.52	76.79	513.90	1496.14	655.86	126.24	11,139.63

*Conversion of ocean area into other land use types was not included.

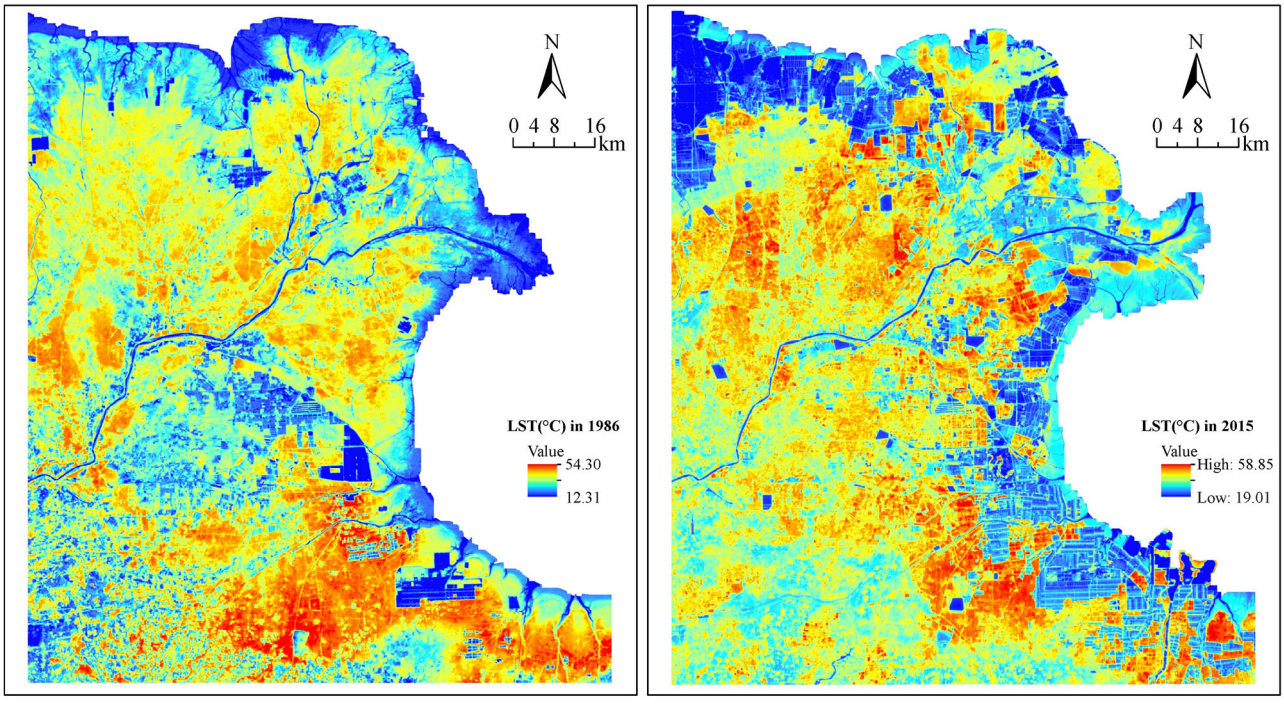

Fig. 3 Distribution maps of LST on June 5, 1986 and 2015.

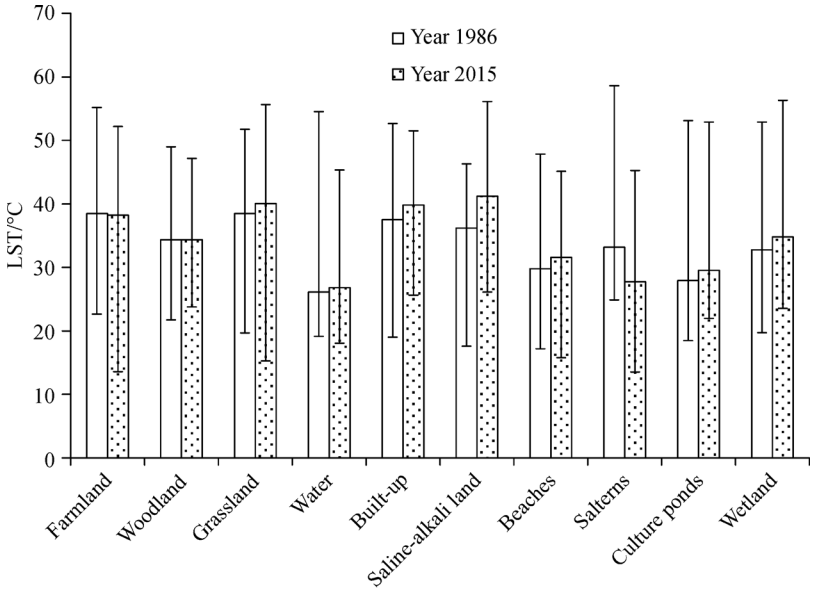

Fig. 4 LST of different land use types on June 5, 1986 and 2015.

coastal areas and it increases with distance from the coastline. However, when the distance increases beyond a certain stage, the LST begins to decrease. This phenomenon is related closely to the spatial distribution of LULC. In order to study the influence of land cover type on LST, the mean LST of different land cover types was obtained via spatial overlay analysis (Fig. 4). The results showed that the mean LST of water areas and aquaculture ponds is lower, while that of saline-alkali fields, grassland, and built-up areas is higher. The heat capacity of water is larger than soil, which causes the temperature of a water body and aquaculture ponds to rise more slowly. The LST of farmland, grassland, saline-alkali fields, and built-up areas was always above 35°C on the two studied days. Because of the hardening of the ground and its small heat capacity, the LST of built-up areas is higher. Saline-alkali fields and grassland are distributed widely throughout the YRD, and their LST is always high because of the sparse vegetation coverage. Although the vegetation coverage of beaches is low, the LST is not that high because of the influences of the sea and shallow ground water.

3.3 Relationship analysis of LULC, LST, and NDVI

The NDVI, as an indicator of vegetation abundance, is the most widely used vegetation index in urban heat island (UHI) research, which uses remote sensing data to estimate the relationship between vegetation and LST. Related data on June 5, 1986 were used as an example. The LST distribution data were discretized by 1°C and the NDVI was discretized to multiples of 0.01. Using a spatial data stack, the corresponding relationship between the LST and the NDVI was obtained (Fig. 5). It can be seen from Fig. 5 that there is no clear linear correlation between LST and the

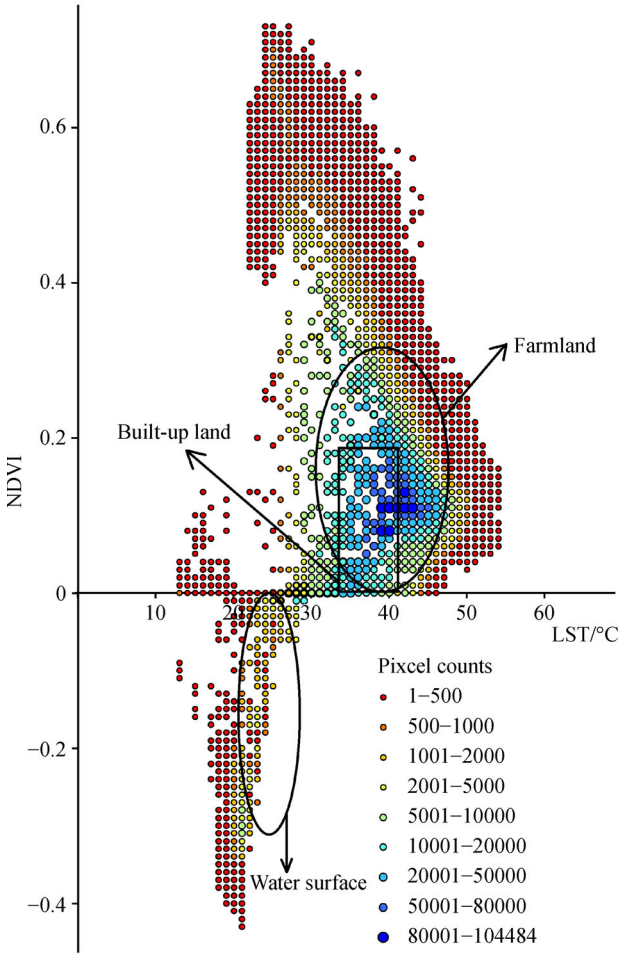

Fig. 5 Spatial relationship between NDVI and LST.

NDVI, although various corresponding relationships exist in different pixels. Sometimes, a numerical correspondence relationship occurs with only one pixel. As mentioned earlier, each pixel is 30 m× 30 m; thus, the largest number of pixels is 104,484 (an area of 94.036 km^2). Considering the spatial correspondence between LST and the NDVI, most pixels are concentrated in the LST range of greater than 30 and less than 40, for which the corresponding NDVI values are between 0.0 and 0.3. Spatial overlap analysis of the land use map allowed the LST and NDVI ranges to be obtained for different land use types. The LSTs of most farmland pixels are 32°C–47°C, corresponding to the NDVI range of 0.00–0.33. This is the most concentrated area of the pixel distribution, which is consistent with previous land use analysis. The LST of the majority of water surfaces ranges from 20°C to 28°C, for which the corresponding NDVI values are 0.00 to –0.33. The LST ranges from 35°C to 41°C in the majority of built-up areas, and the corresponding NDVI values are 0.00–0.18. The land use types with the largest range of LST are saline-alkali fields and salterns, which is attributable to the frequent spatiotemporal variation of the vegetation cover of these two land use types.

3.4 Spatial analysis between LST and the VIs

To some extent, the VIs collectively represent the features of land use, and the LSTs coherently reflect the thermal conditions of the land surface. Consequently, integrating LST with NDVI, ANDVI, SAVI, and MSAVI with appropriate intervals could provide some insightful findings. Our analysis elucidates this supposition by choosing an interval of 0.01 for the VIs and a mean value of LST for the corresponding pixels. Figure 6 shows the relationships between LST and the VIs in the different years of time series A.

Using Fig. 6(a) as an example, the characteristics of the pattern between the NDVI and LST can be described as follows. 1) An NDVI value of 0.10 is the inflection point in 1986 (0.13 in 1996, 0.21 in 2015), 2) The LST and the NDVI are correlated positively (R^2: 0.94 in 1986, 0.95 in 1996, and 0.96 in 2015) when the value of the NDVI is 0.00–0.10 in 1986 (0.00–0.13 in 1996, 0.00–0.21 in 2015). 3) Generally, the LST and the NDVI are correlated negatively (R^2: 0.96 in 1986, 0.91 in 1996, and 0.97 in 2015) when the NDVI is 0.10–0.75 in 1986 (0.13–0.60 in 1996, 0.21–0.75 in 2015). 4) When the NDVI is 0.41–0.53 in 1986 (0.44–0.55 in 1996), there is little change in LST.

In general, the NDVI value increases with enhanced vegetation coverage. It is easy to understand that higher vegetation coverage would lead to lower LST; however, when the NDVI is below a certain value, the LST appears to increase with the VI. Through comparative analysis of the NDVI and the spatial distribution map of land use, it is found that NDVI values in the range 0.00–0.10 (the inflection point) in 1986 are associated mainly with coastal areas covered by beaches, wetland, saline-alkali fields,

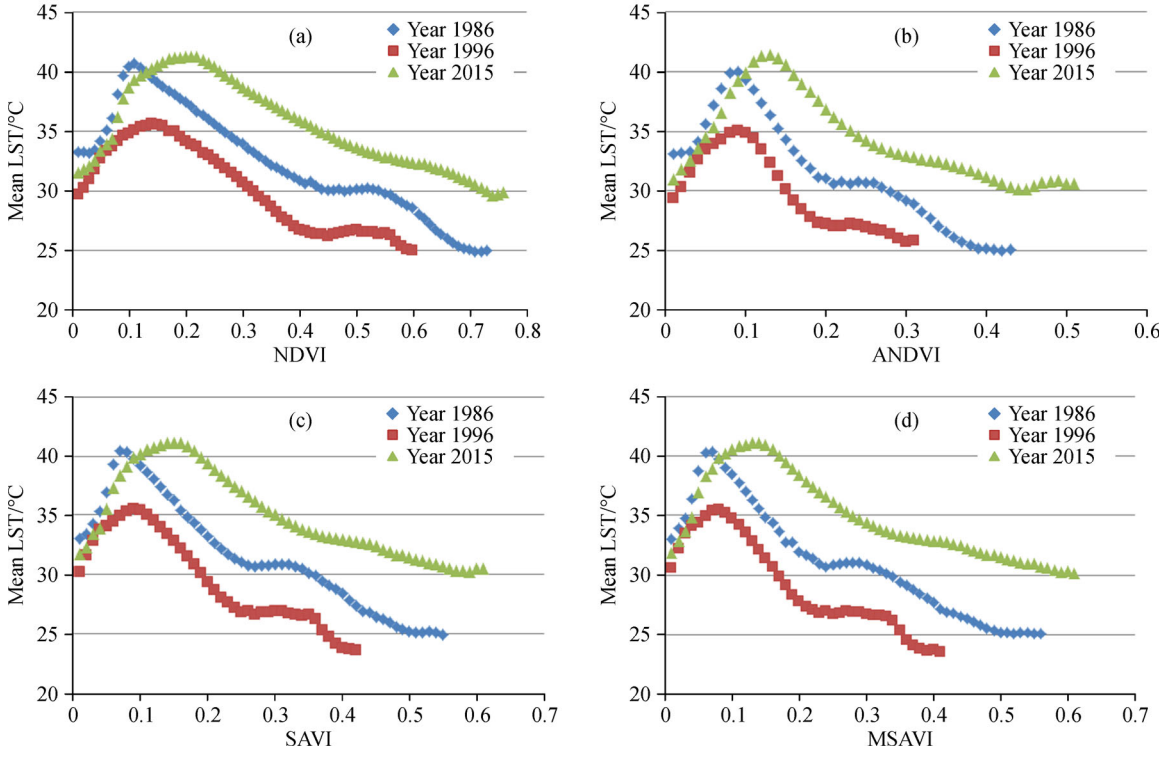

Fig. 6 Relationships between mean LST and the VIs (time series A).

salterns, and aquaculture ponds. Coastal areas with NDVI values of 0.00–0.10 were selected to investigate the positive correlation between LST and the NDVI. To facilitate the analysis, coastal areas with NDVI values in the target range were divided into three parts based on thresholds of 0.02 and 0.07, as shown in Fig. 7(a). The seawater temperature was lower than the land temperature at the time of acquisition of the Landsat images, and the closer the proximity to the sea, the greater the influence of the seawater temperature (Fig. 7(b)). The LST of the coastal zone shows an increasing trend from sea to land, while the vegetation coverage and NDVI also increased. The LST and the NDVI show positive correlation. Thus, it can be concluded that the influence of seawater temperature makes the correlation of the LST–NDVI relationship positive in coastal areas. A similar conclusion can be drawn from the study of other VIs and the spatial distribution of LST.

Similar results can be concluded based on Figs. 6(b)–6(d). When the values of the ANDVI, SAVI, and MSAVI are lower than the inflection point, the LST and the VIs are correlated positively, and vice versa. In time series A, the inflection point value of the VI in 1996 is always a little larger than in 1986, and that of 2015 is the largest of the three.

The relationships between mean LST and the VIs for the years in time series B were also analyzed. As shown in Fig. 8, the correlation between LST and the VIs in time series B was similar to time series A. The LST and VIs show positive correlations when the values of the VIs are lower than the inflection point, and vice versa.

4 Discussion

During the last 30 years, land use in the YRD has been transformed. Overall, the transformation has occurred primarily from poorly utilized land into highly utilized land. The drastic change in land use types has inevitably affected the distribution and transformation of regional energy. The selected images of each time series have similar astronomical dates, making it possible to compare the LST of different years. It should be noted that precipitation, air temperature, humidity, and wind speed at the time of acquisition would have had an important impact on the instantaneous LST.

With increasing distance from sea, the vegetation coverage rate and the NDVI spatially showed increasing trends, closely related to the distribution of land use (Figs. 2 and 3). The mean NDVI in the study area showed an increasing trend, but the mean LST changed differently under the influence of weather conditions. It must be emphasized that the VIs and LST showed a more complex relationship in 1984 in time series B (Fig. 8). The relationship of LST and the NDVI in 1984 is displayed as an example in Fig. 9(a). When the NDVI value is > 0.15, the LST is correlated negatively with the NDVI, which is similar to other years. When the NDVI value is < 0.15, there are two new turning points (0.04 and 0.09). When the NDVI value is > 0.04 and < 0.09, the LST and NDVI show a negative relationship, which is contrary to that of other years. In order to facilitate further analysis, NDVI values in the range 0.04–0.09 were divided into two parts based on the threshold value 0.064 (Fig. 9(b)). A change of the LST in the same region is evident in Fig. 9(c). Therefore, we investigated the meteorological conditions for the 10 days before the acquisition of the Landsat imagery using data from the Kenli weather station (within the study area). It was found that precipitation occurred on the third and seventh days before the acquisition date in 1984 (1.7 and 18.1 mm, respectively), whereas precipitation during the 10 days prior to the acquisition of the remaining images was zero. The precipitation in 1984 just before image acquisition would have improved the soil moisture content in coastal low-lying areas and thus, decreased the corresponding LST.

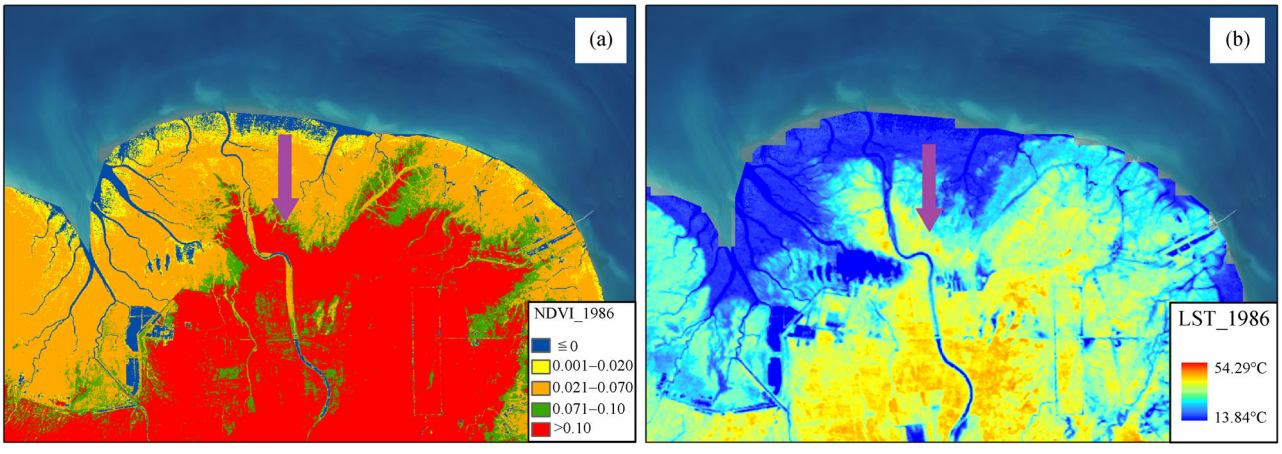

Fig. 7 Distribution map of (a) NDVI and (b) LST changes with the distance to the sea in coastal zone areas.

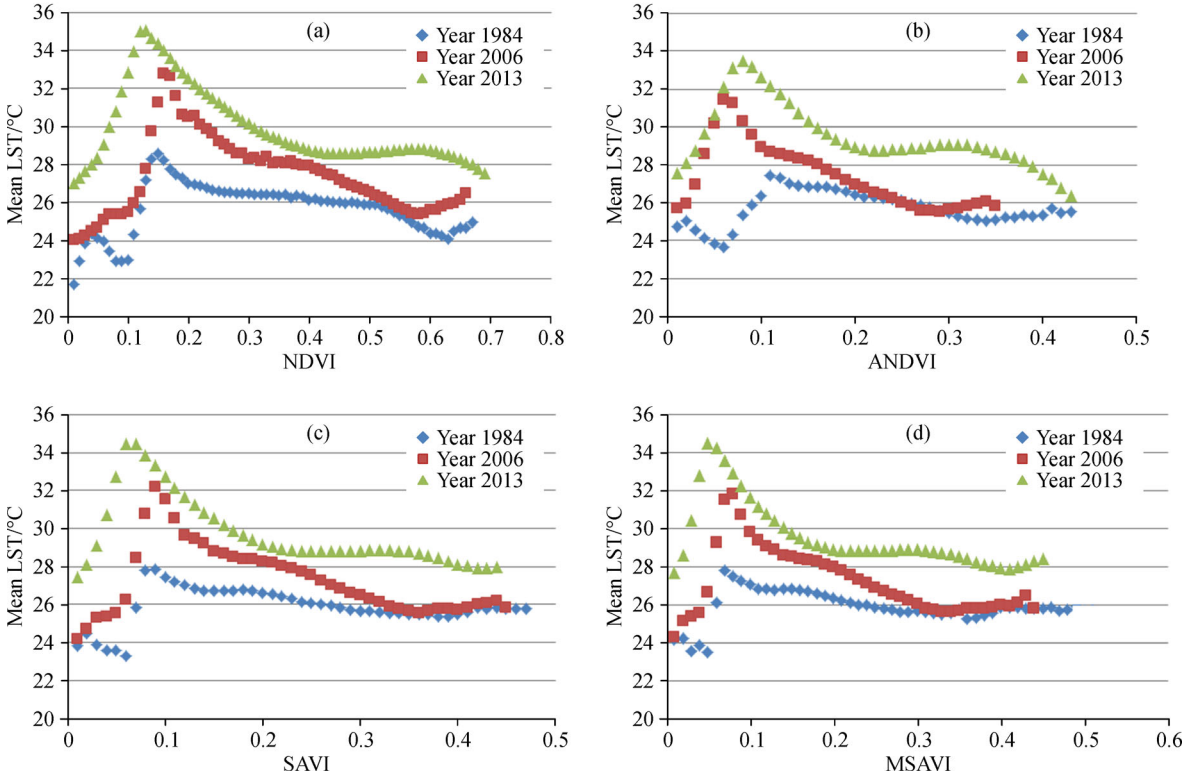

Fig. 8 Relationships between mean LST and the VIs (time series B).

Because LST is sensitive to soil moisture content, the sensitivity of LST to the soil water content should be analyzed under certain conditions. If conditions permit, the effects of the magnitude and time interval of antecedent precipitation should be considered in detail.

Schwarz et al. (2012) suggested that the nonlinearity of the NDVI might make it unsuitable as an indicator for quantitative analyses of vegetation when investigating the vegetation–LST relationship. The relationship between the LST and NDVI should be calibrated further. Mroz and Sobieraj (2004) also suggested seeking a more suitable and robust vegetation abundance indicator to supersede NDVI in vegetation–LST relationship studies. Interestingly, we have obtained improved results through the application of specific data processing methods; however, some remaining problems deserve further attention. In order to facilitate data processing and analysis of results, artificial auxiliary interpretation and the mean LST were used, which to some extent ignore the detail. Although LULC can affect LST, there are certain differences in LST between different vegetation and land cover types. For any given spatio-temporal condition, there is a close relationship between a VI and LST. However, because a VI is a concentrated embodiment of vegetation form, structure, soil regime, and other relevant essential factors, the particular situation should be taken into consideration if the change of LST is studied in relation to the VI. In addition, a simple classification of vegetation cover is also bound to smooth some of the detail.

5 Conclusions

From 1986 to 2015, the YRD has experienced an increase in land area of 205.81 km^2 because of sediment deposition. Research on LULC has indicated that an area of 3948 km^2 of various land use types changed from 1986 to 2015, accounting for 35.04% of the total land area in 1986. Despite an increase in the gross area, a large area of farmland and grassland has been converted into salterns and aquaculture ponds. The decreased diversity of wetland emphasizes the fragility of wetland ecosystem. The exploitation of saline-alkali fields is also one of the primary means of conversion of land use types within the YRD area. Overall, conversion generally occurs from poorly utilized land into highly utilized land.

There is close correlation between LST and vegetation coverage. Through analysis of the relationship between LST and different VIs, it was found that different inflection points exist. When the values of the NDVI, ANDVI, SAVI, and MSAVI are greater than the inflection point, LST and the VIs are correlated negatively. When the VIs values are lower than the inflection points, it is always the coastal areas distributed by land use types of beaches, wetlands,

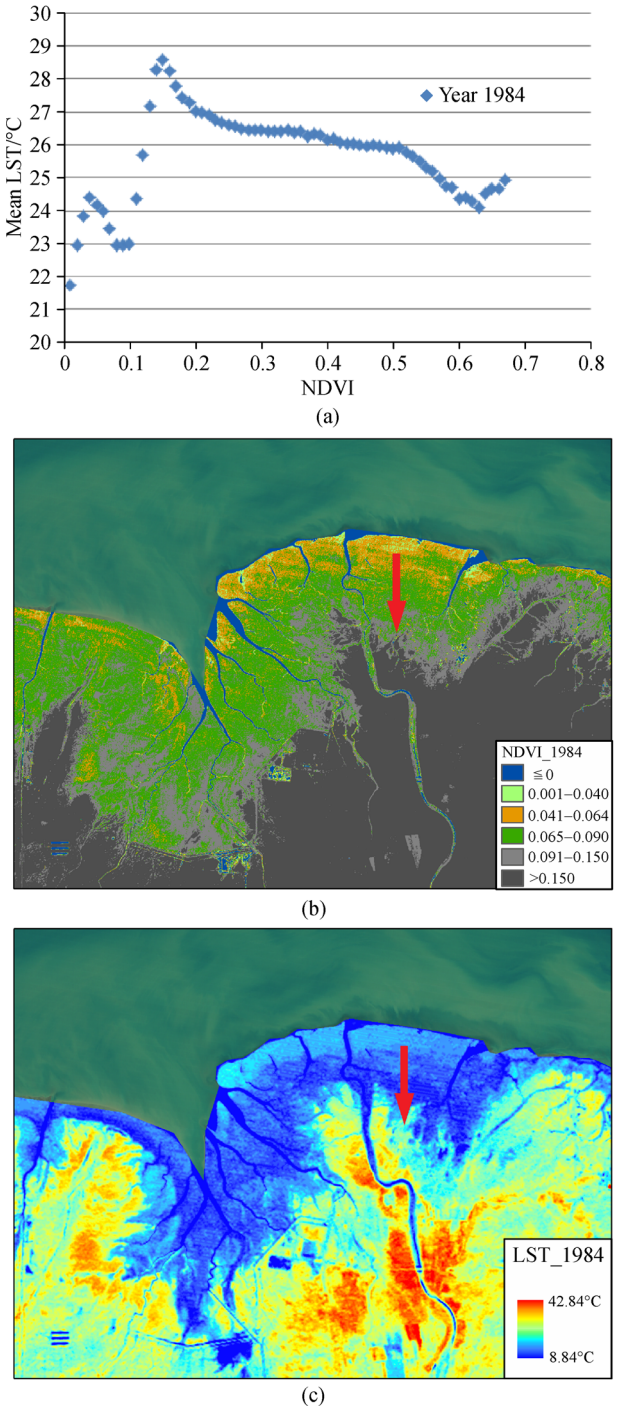

Fig. 9 Example area of coastal zone in 1984. (a) Relationships between mean LST and NDVI. (b) Distribution map of NDVI. (c) Distribution map of LST.

and saline-alkali fields. The LST of coastal areas is affected greatly by local seawater temperature, and it showed a positive relationship with the VIs. Weather conditions such as precipitation were also found to affect the change of LST.

Acknowledgements The authors are grateful for the support of the Science and Technology Project of Yantai (No. 2014ZH085). This work was also supported by the Aoshan Science and Technology Innovation Program of Qingdao National Laboratory for Marine Science and Technology (2016ASKJ02), Strategic Priority Research Program of the Chinese Academy of Sciences (CAS) (XDA11020702), Basic Special Program of Ministry of Science and Technology (2014FY210600), Youth Innovation Promotion Association of CAS (2016195), and Key Research Program of the Chinese Academy of Sciences (KZZD-EW-14).

References

Bhattacharya B K, Mallick K, Patel N K, Parihar J S (2010). Regional clear sky evapotranspiration over agricultural land using remote sensing data from Indian geostationary meteorological satellite. J Hydrol (Amst), 387(1−2): 65–80

Bi N H, Wang H J, Yang Z H (2014). Recent changes in the erosion–accretion patterns of the active Huanghe (Yellow River) delta lobe caused by human activities. Cont Shelf Res, 90: 70–78

Blum M D, Roberts H H (2009). Drowning of the Mississippi Delta due to insufficient sediment supply and global sea–level rise. Nat Geosci, 2(7): 488–491

Brunsell N A (2006). Characterization of land–surface precipitation feedback regimes with remote sensing. Remote Sens Environ, 100 (2): 200–211

Buyadi S N A, Mohd W M N W, Misni A (2013). Impact of land use changes on the surface temperature distribution of area surrounding the National Botanic Garden, Shah Alam. Procedia Soc Behav Sci, 101: 516–525

Chen X L, Zhao H M, Li P X, Yin Z Y (2006). Remote sensing image-based analysis of the relationship between urban heat island and land use/cover changes. Remote Sens Environ, 104(2): 133–146

Cheng K S, Su Y F, Kuo F T, Hung W C, Chiang J L (2008). Assessing the effect of landcover on air temperature using remote sensing images—A pilot study in northern Taiwan. Landsc Urban Plan, 85 (2): 85–96

Cui B S, Yang Q C, Yang Z F, Zhang K J (2009). Evaluating the ecological performance of wetland restoration in the Yellow River Delta, China. Ecol Eng, 35(7): 1090–1103

Dash P, Göttsche F M , Olesen F S , Fischer H (2002). Land surface temperature and emissivity estimation from passive sensor data: theory and practice—current trends. Int J Remote Sens, 23(13): 2563–2594

Fall S, Niyogi D, Gluhovsky A, Pielke R A Sr, Kalnay E, Rochon G (2010). Impacts of land use land cover on temperature trends over the continental United States: assessment using the North American Regional Reanalysis. Int J Climatol, 30(13): 1980–1993

Friedl M A (2002). Forward and inverse modeling of land surface energy balance using surface temperature measurements. Remote Sens Environ, 79(2−3): 344–354

Gao M S, Liu S, Zhao G M, Yuan H M, Wei C B, Wu Y H, Tang J H (2014). Vulnerability of eco-hydrological environment in the Yellow River Delta wetland. J Coast Res, 294(2): 344–350

Huete A R (1988). A soil-adjusted vegetation index (SAVI). Remote Sens Environ, 25(3): 295–309

Jimenez-Munoz J C, Sobrino J A, Skokovic D, Mattar C, Cristobal J (2014). Land surface temperature retrieval methods from Landsat-8 thermal infrared sensor data. IEEE Geosci Remote Sens Lett, 11(10): 1840–1843

Jin Y, Yang W, Sun T, Yang Z, Li M (2016). Effects of seashore reclamation activities on the health of wetland ecosystems: a case study in the Yellow River Delta, China. Ocean Coast Manage, 123: 44–52

Kong D X, Miao C Y, Borthwick A G L, Duan Q Y, Liu H, Sun Q H, Ye A Z, Di Z H, Gong W (2015). Evolution of the Yellow River Delta and its relationship with runoff and sediment load from 1983 to 2011. J Hydrol (Amst), 520: 157–167

Kumar D, Shekhar S (2015). Statistical analysis of land surface temperature–vegetation indexes relationship through thermal remote sensing. Ecotoxicol Environ Saf, 121: 39–44

Li Z L, Tang B H, Wu H, Ren H, Yan G, Wan Z, Trigo I F, Sobrino J A (2013). Satellite-derived land surface temperature: current status and perspectives. Remote Sens Environ, 131(8): 14–37

Liang S, Fang H, Morisette J T, Chen M, Shuey C J, Walthall C (2002). Atmospheric correction of Landsat ETM+ land surface imagery: II. validation and applications. IEEE Transactions on Geoscience & Remote Sensing, 40(12): 1–10

Liu Z Y, Huang J F, Wang F M, Wang Y (2008). Adjusted-Normalized Difference Vegetation Index for estimating leaf area index of rice. Scientia Agricultura Sinica, 41(10): 3350–3356

Lv Z Q, Zhou Q G (2011). Utility of Landsat image in the study of land cover and land surface temperature change. Procedia Environ Sci, 10 (1): 1287–1292

Mroz M, Sobieraj A (2004). Comparison of several vegetation indices calculated on the basis of a seasonal SPOT XS time series, and their suitability for land cover and agricultural crop identification. Technical Sciences, 7: 39–66

Ottinger M, Kuenzer C, Liu G, Wang S, Dech S (2013). Monitoring land cover dynamics in the Yellow River Delta from 1995 to 2010 based on Landsat 5 TM. Appl Geogr, 44(4): 53–68

Pal S, SkZiaul (2017). Detection of land use and land cover change and land surface temperature in English Bazar urban centre. Egypt J Remote Sens Space Sci, 20(1): 125–145

Petropoulos G P, Griffiths H M, Kalivas D P (2014). Quantifying spatial and temporal vegetation recovery dynamics following a wildfire event in a Mediterranean landscape using EO data and GIS. Appl Geogr, 50(2): 120–131

Pielke R A Sr, Avissar R, Raupach M, Dolman A J, Zeng X, Denning A S (1998). Interactions between the atmosphere and terrestrial ecosystems: influence on weather and climate. Glob Change Biol, 4(5): 461–475

Pu R, Gong P, Michishita R, Sasagawa T (2006). Assessment of multi-resolution and multi-sensor data for urban surface temperature retrieval. Remote Sens Environ, 104(2): 211–225

Qi J, Chehbouni A, Huete A R, Kerr Y H, Sorooshian S (1994). A modified soil adjusted vegetation index. Remote Sens Environ, 48(2): 119–126

Qin Z, Karnieli A, Berliner P (2001a). A mono-window algorithm for retrieving land surface temperature from Landsat TM data and its application to the Israel–Egypt border region. Int J Remote Sens, 22 (18): 3719–3746

Qin Z, Li W, Xu B, Chen Z X, Liu J (2004). The estimation of land surface emissivity for Landsat TM6. Remote Sensing for Land & Resources, 16(3): 28–41

Qin Z, Zhang M, Karnieli A, Berliner P (2001b). Mono-window algorithm for retrieving land surface temperature from Landsat TM6 data. Acta Geogr Sin, 56(4): 456–466

Rhee J, Park S, Lu Z (2014). Relationship between land cover patterns and surface temperature in urban areas. Geoscience & Remote Sensing, 51(5): 521–536

Rozenstein O, Qin Z, Derimian Y, Karnieli A (2014). Derivation of land surface temperature for Landsat-8 TIRS using a split-window

algorithm. Sensors (Basel), 14(4): 5768–5780

Sahana M, Ahmed R, Sajjad H (2016). Analyzing land surface temperature distribution in response to land use/land cover change using split window algorithm and spectral radiance model in sundarban biosphere reserve, india. Modeling Earth Systems and Environment, 2(2): 81

Schwarz N, Schlink U, Franck U, Großmann K (2012). Relationship of land surface and air temperatures and its implications for quantifying urban heat island indicators—An application for the city of Leipzig (Germany). Ecol Indic, 18(4): 693–704

Sobrino J A, Jiménez–Muñoz J CPaolini L (2004). Land surface temperature retrieval from Landsat TM 5. Remote Sens Environ, 90 (4): 434–440

Syvitski J P M, Kettner A J, Overeem I, Hutton E W H, Hannon M T, Brakenridge G R, Day J, Vorosmarty C, Saito Y, Giosan L, Nicholls R J (2009). Sinking deltas due to human activities. Nat Geosci, 2(10): 681–686

USGS (2014). Landsat 8 reprocessing to begin February 3, 2014.https://landsat.usgs.gov/landsat-8-l8-operational-land-imager-oli-and-thermal-infrared-sensor-tirs

Wang H J, Yang Z S, Saito Y, Liu J P, Sun X X (2006). Interannual and seasonal variation of the Huanghe (Yellow River) water discharge over the past 50 years: connections to impacts from ENSO events and dams. Global Planet Change, 50(3−4): 212–225

Wang S, Ma Q, Ding H, Liang H (2016). Detection of urban expansion and land surface temperature change using multi-temporal Landsat images. Resour Conserv Recycling, doi: 10.1016/j.resconrec.2016.05.011

Wei M A, Zhou J (2011). Quantitative analysis of land surface temperature–vegetation indexes relationship based on remote sensing. The International Archives of the Photogrammetry, Remote Sensing and Spatial Information Sciences. Vol. XXXVII. Part B6b. Beijing

Weng Q, Lu D, Schubring J (2004). Estimation of land surface temperature–vegetation abundance relationship for urban heat island studies. Remote Sens Environ, 89(4): 467–483

Windahl E, Beurs K D (2016). An intercomparison of Landsat land surface temperature retrieval methods under variable atmospheric conditions using in situ skin temperature. Int J Appl Earth Obs Geoinf, 51: 11–27

Yokohari M, Brown R D, Kato Y, Yamamoto S (2001). The cooling effect of paddy fields on summertime air temperature in residential Tokyo, Japan. Landsc Urban Plan, 53(1−4): 17–27

Yu X, Guo X, Wu Z (2014). Land surface temperature retrieval from Landsat 8 TIRS—comparison between radiative transfer equation-based method, split-window algorithm and single-channel method. Remote Sens, 6(10): 9829–9852

Yue W, Xu J, Tan W, Xu L (2007). The relationship between land surface temperature and NDVI with remote sensing: application to Shanghai Landsat 7 ETM+ data. Int J Remote Sens, 28(15): 3205–3226

Zhang H, Chen X, Luo Y (2016). An overview of ecohydrology of the Yellow River delta wetland. Ecohydrology & Hydrobiology, 16(1): 39–44